Secondary vortex street in the wake of two tandem circular cylinders at low Reynolds number

Si-ying Wang, Fang-bao Tian, Lai-bing Jia, Xi-yun Lu, and Xie-zhen Yin[*]

Department of Modern Mechanics, University of Science and Technology of China, Hefei, Anhui 230027, China

The experiments on two tandem circular cylinders were conducted in a horizontal soap film tunnel for the Reynolds number Re=60, 80, and 100 and the nondimensional center-to-center spacing Γ ranging in $1 \sim 12$. The flow patterns were recorded by a high-speed camera and the vortex shedding frequency was obtained by a spatiotemporal evolution method. The secondary vortex formation (SVF) mode characterized by the formation of a secondary vortex street in the wake of the downstream cylinder was found at large Γ. Moreover, some typical modes predicted by previous investigations, including the single bluff-body, shear layer reattachment, and synchronization of vortex shedding modes, were also revisited in our experiments. Further, numerical simulations were carried out using a space-time finite-element method and the results confirmed the existence of the SVF mode. The mechanism of SVF mode was analyzed in terms of the numerical results. The dependence of the Strouhal number Sr on Γ was given and the flow characteristics relevant to the critical spacing values and the hysteretic mode transitions were investigated.

I. INTRODUCTION

Analysis of flow structures around arranged bluff bodies is a common problem in a variety of engineering applications such as the flow past tall buildings and tube banks in heat exchanger. For flow around tall buildings, it is needed to suppress the vortex shedding in order to reduce the total drag and to minimize the unsteady aerodynamic loads. In the heat exchanger, the aim is to increase the heat transfer efficiency and to decrease the induced vibration and fatigue damage. The understanding of the flow behaviors and the aerodynamic loads on the bluff bodies is significantly important in fundamentals and applications. To deal with the flow interaction between bodies, some arrangements, such as side-by-side, in-line, or staggered in the uniform flow, were investigated extensively. Considering flow over two tandem identical circular cylinders, most of the early experiments were conducted in wind or water tunnels to observe the flow patterns using a smoke or dye visualization. The unsteady loads on cylinders and the frequency of vortex shedding were studied using a hot-wire anemometer, surface pressure measurement or aerodynamic balance. Recently, much more effort has been devoted to study the flow characteristics and to reveal the mechanism of the mode transitions.

The flow around two tandem circular cylinders mainly depends on two governing parameters: the Reynolds number Re=Ud/ν (U is the oncoming flow velocity, d the cylinder diameter, and ν the kinematic viscosity) and the nondimensional spacing Γ=L/d (L center-to-center distance between both the cylinders). Zdravkovich [1,2] conducted smoke visualization experiments in a vertical wind tunnel and identified six different flow patterns around two tandem cylinders at Re=$8 \times 10^4 \sim 1.1 \times 10^5$. Tanida *et al.* [3] measured the lift and drag on two cylinders arranged in-line at Re=$40 \sim 10^4$ and found that the forces depend strongly on the spacing and the Reynolds number. Igarashi [4,5] reported the results of

the mean drag and heat transfer of two tandem circular cylinders at Re=$3.3 \times 10^3 \sim 6.0 \times 10^4$. With the development of experimental techniques, some experiments [6–11] were fulfilled for a wider range of Re and Γ. Numerical simulations [12–16] were also employed to study the relevant problem.

Different flow patterns were classified based on the flow field structure, the vortex shedding frequency and the forces acting on the cylinders. Sumner *et al.* [6] provided detailed identification on the flow patterns for two staggered cylinders in a cross flow at $850 < \text{Re} < 1900$, including single bluff-body (SBB) flow, shear layer reattachment (SLR), and synchronization of vortex shedding (SVS) modes for two cylinders in tandem. In the SBB mode with small spacing Γ ($< 1.2 - 1.8$, depending on Re), the two cylinders act like one bluff body. The vortices shed from the upstream cylinder overshoot the downstream one and form a Karman vortex street in the wake. For $1.2 - 1.8 < \Gamma < 3.4 - 3.8$, the shear layers separating from the upstream cylinder reattach to the surface of the downstream one and form a Karman vortex street behind it, which is called SLR mode. When Γ is larger than the critical spacing Γ_c, both the cylinders shed vortices at the same frequency, named as SVS mode. Here Γ_c is the spacing range lying in the SLR and SVS modes and is associated with Re. For instance, Tanida *et al.* [3] found the value of Γ_c is 5 at Re=80 and 3 at Re=3400. Recently, Kuo *et al.* [11] focused on the flow field between the two cylinders and studied the self-sustained oscillatory flow mode between the SLR and SVS modes at Re=1000. Two symmetric unstable shear layers occur between the two cylinders at $4.5 < \Gamma < 5.5$ and the upstream cylinder starts to shed vortices at Γ_c=6.

When the upstream cylinder starts to shed vortices at the critical spacing Γ_c, the value of the nondimensional frequency Sr=fd/U, where f is the vortex shedding frequency, suffers a jump. Many researchers have studied the dependency of Γ_c and Sr on Re experimentally [1–11] and numerically [12–16]. However, previous studies only have focused on either the Sr-Re or Sr-Γ relationship for a limit range of Γ and Re. Few experimental work concerned the flow field around two tandem cylinders at relatively low Re ($< 3 \times 10^3$).

---

*Corresponding author; xzyin@ustc.edu.cn

Mizushima and Suehiro [17] studied the instability and transition of the flow modes for two tandem cylinders at low Re using linear stability analysis and numerical simulation. They first predicted the bifurcation diagram and the hysteretic exchanges between different vortex shedding modes and found that there exists a certain range of gap where the physical quantities show an abrupt change with Re continuously changed. The origin of such abrupt change is explained by the existence of multiple stable solutions for the flow. Then, Tasaka *et al.* [18] conducted an experiment of flow visualizations and velocity measurements on two tandem cylinders in a water tunnel. The experimental results basically verified the theoretical predictions except for some slight differences in the ranges and transition values of Re and Γ, which was attributed to the finite length of the cylinders used in experiments.

Besides the lack of experimental data at low Re, the previous researchers mainly focused on the flow structures in the near wake of the cylinders and little work was done regarding the flow structure in the far wake behind the downstream cylinder. In previous experiments conducted in wind or water tunnels, the traditional visualization method usually used smoke or dye emitted from a fixed location to present streak lines. This approach is difficult to visualize clearly the far downstream flow due to the viscous dissipation. The flow visualization of streak lines may often mislead investigators as proved by Cimbala *et al.* [19]. Moreover, the far downstream flow is also rarely calculated in numerical simulations.

In order to study the flow around two tandem cylinders at low Reynolds number, we accomplished the experiments on two tandem cylinders in a soap film tunnel and investigated the evolution of the far wake using a high-speed video camera. The soap film tunnel is a convenient platform for two-dimensional experiments and has advantage in far wake visualization, as proved by the extensive hydrodynamic experiments [20–22]. A time-space finite element method was also employed to simulate this problem.

This paper is organized as follows. The experiment set-up and parameter measurements are presented in Sec. II. Then we describe the experimental results in Sec. III and the numerical results in Sec. IV. The SVF mode of the formation of the secondary vortex street is analyzed in Sec. V and the Sr-Γ relationships and the hysteretic mode transitions are exhibited in Sec. VI. Finally a brief conclusion is given.

II. EXPERIMENTAL SET UP

Our experiments were carried out in a horizontal soap film tunnel, which was recently developed in our laboratory referring to the gravity-driven soap film tunnel designed by Georgiev and Vorobieff [23]. A sketch of the experimental set up is shown in Fig. 1.

A mixture of 95% water and 5% liquid detergent was pumped into the upper reservoir. The reservoir contains an overflow to maintain a fixed pressure head. A stopcock is fixed at the exit of the upper reservoir to control the flux and the corresponding flow speed. Two nylon threads with diameter 1.5 mm connect the upper reservoir to the lower one.
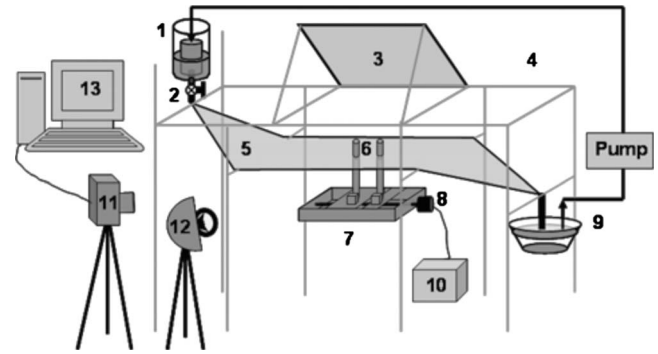

FIG. 1. Sketch of the experimental system. [(1) upper reservoir, (2) stopcock, (3) mirror, (4) frame, (5) soap film, (6) cylinders, (7) linear stage, (8) driver, (9) lower reservoir, (10) dc power, (11) high-speed video camera, (12) sodium lamps, (13) computer.]

Driven by gravity, the surfactant solution will flow down along the two nylon threads, forming a soap film between them and finally stream back into the lower reservoir. As shown in Fig. 1, the whole soap film consists of the expanding, testing, and contracting sections. When the solution is injected through the stopcock, the soap film is accelerated by gravity, but soon slows down due to the air resistance and reaches its steady velocity state in the test section. The length of the horizontal testing section is 1.1 m and the width is 0.1 m. The flow speed U in the test section of this soap film tunnel can be changed continuously using the stopcock and it ranges from 0.3 to 1.6 m/s measured by a particle tracing velocimetry (PTV) method. In our experiment, the flow velocity was retained at $U=0.8$ m/s.

Trapeznikov [24] first applied the method of two-dimensional viscosity and shear strength to investigate the structure and composition of two-sided films and surface layers in solutions of soaps and saponins. Chomaz [25] proved that the leading-order equations describing the soap film commendably correspond to the equations of the two-dimensional fluid dynamics on the basis of appropriate physical considerations. When the flow velocity is much lower than the Marangoni elastic wave speed and the initial nonuniformity of the film thickness is small, the soap film flow corresponds to the two-dimensional incompressible Navier-Stokes equation and the variation of its thickness represents the velocity field. When the flow velocity is larger than the elastic wave speed and the fluid viscosity and the surfactant solubility are negligible, the soap film flow corresponds to the compressible Euler equations. In the present experiment, the flow speed retained 0.8 m/s, much smaller than the Marangoni elastic wave speed (about 10 m/s). Meanwhile, as the interference fringes proved that the initial film thickness is uniform in the test section, so the flow in the soap film could be considered as a two-dimensional incompressible flow. Our previous experiment conducted in the same soap film tunnel shows that the threshold Reynolds number for a cylinder in uniform flow to shed vortices is 44–50, consistent with our numerical and the two-dimensional (2D) theoretical results.

Three high pressure sodium lamps, which were connected to each phase of the ac power, were adopted to illuminate the
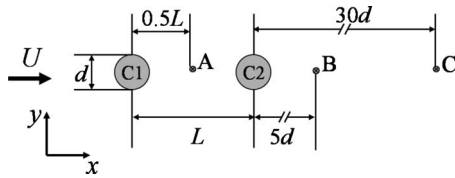
FIG. 2. Coordinates and symbols.

test section of the soap film. Since the thickness of the film is close to the wavelength of the light emitted from the sodium lamp, the interference fringes of the light rays reflected from the two liquid-air interfaces of the soap film can visualize the thickness variation of the film and represent the velocity field of the soap film flow. The experimental images were recorded by a high-speed video camera (Weinberger Speed CAMpro) and a digital camera (Minolta DiMAGE 7i). The frequency of the high-speed camera retained 2004 frames per second.

Figure 2 shows the coordinates and symbols used in the experiments. Two tandem identical cylinders were placed in the test section along the incoming flow direction. The upstream cylinder C1 was fixed and the downstream one C2 was set onto a linear stage driven by a motor. The center-to-center spacing L between them varied from $1d$ to $12d$ and then went back to $1d$ by adjusting the position of the stage. The changing speed of Γ was exactly small, which is less than 0.2 mm/s, about 0.25‰ of the uniform flow speed. In addition, we repeated the same experiments with C2 fixed and C1 moved and identified that the results showed no obvious difference.

The frequency of vortex shedding at three special positions A, B, and C in the flow field was analyzed. As shown in Fig. 2, the position A lies in the middle of both the cylinders, and B and C are $5d$ and $30d$ behind the center of C2, respectively.

In order to calculate the vortex shedding frequency, we exploited a so-called "spatiotemporal evolution" (STE) software package. Figure 3 shows the procedure to make STE pictures. First, as shown in Fig. 3(a), a strip being 3 pixels wide was cut from each photo taken by the high-speed video camera at a certain position marked by the black triangle.
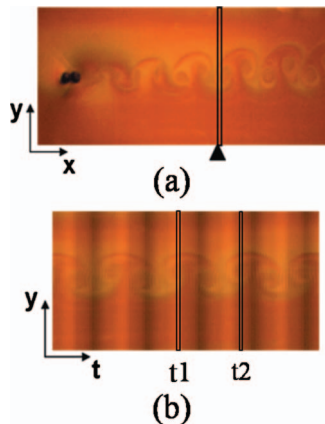
Second, all the strips were ranked in series on the time axis as shown in Fig. 3(b), in which the rightward of the abscissa is the direction of time increasing. The synthesized picture vividly exhibits the periodic pattern of the wake evolution at that position such as a photo recorded by a streak camera. Here the periodic brightness variation of the whole vertical strips in Fig. 3(b) is attributed to the variation light intensity of the lamps. Finally, using an image framing software we could easily count the number N of the columns between t_1 and t_2 in the STE picture, which is also the amount of the pictures taken in an entire period. The period equals the interval 1/2004 s times N and then the vortex shedding frequency could be calculated.

Usually, it is difficult to determine the Reynolds number in soap film experiments since the kinematic viscosity ν of the composite soap solution is related to the thickness and the flow speed of the soap film. In the present study, we used a commonly used approach to predict the kinematic viscosity. For a single circular cylinder, the Reynolds number can be inferred from the Strouhal number Sr, assuming that the Re-Sr relationship is known. Previous work [26,27] used the empirical Re-Sr relationship given in [28] to determine Re based on the measured value of Sr, and then predicted the kinematic viscosity using $\nu=\frac{Re}{Ud}$. Here, we used the similar method but with a more update accurate Re-Sr relation, which is based on the observation of the vortex street structure in a flowing soap film by Roushan and Wu [29]. The expression is $Sr=\frac{1}{5.12+113/Re}$. For $U=0.8$ m/s in our experiment, the vortex shedding frequencies of single circular cylinder with $d=2.5$, 2.0, and 1.5 mm were measured and then the corresponding Reynolds numbers were calculated from the Sr-Re relation. Finally, the mean value of the kinematic viscosity was obtained as $\nu=2.0\times10^{-5}$ m²/s and the Reynolds number based on the diameter of cylinder was 100, 80, and 60, corresponding to three cylinders with the diameter 2.5, 2.0, and 1.5 mm.

III. EXPERIMENTAL RESULTS

A. Flow modes

In our experiment, when the spacing between the two cylinders increases, a series of flow patterns (i.e., SBB, SLR, and SVS) were observed successively.
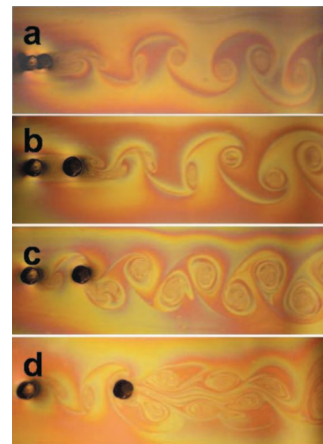

FIG. 4. (Color) Flow fields. (a) SBB, (b) SLR, (c) SVS, and (d) SVF.

FIG. 3. (Color) Spatiotemporal evolution method. (a) Cut strips from images and (b) synthesize evolution image using the strips.

1. SBB mode

When the two circular cylinders are very close ($\Gamma < 2.0$), the SBB mode occurs. The shear layers separated from the upstream cylinder C1 overshoot the downstream cylinder C2 and form a vortex street behind C2. The flow structure in Fig. 4(a) exhibits a similar flow pattern as the flow around a single bluff body. The Karman vortex street in the wake is stable and the frequency of vortex shedding reduces rapidly as Γ increases.

2. SLR mode

When the spacing between the cylinders increases, as shown in Fig. 4(b), the shear layers separated from C1 reattach to the surface of C2 and form a region of circumfluence between both the cylinders. There exists only one Karman vortex street behind C2. Although no vortex shedding occurs on C1, the flow between the two cylinders is nonuniform. The frequencies of vortex shedding are obviously identical at positions B and C as same as in SBB mode. But the interaction of the long shear layers makes the vortex street not so stable as in the SBB mode, especially for large Γ. For this difference in the stability, Kuo *et al.* [11] subdivided the SLR mode into two submodes: for smaller Γ, two smooth shear layers separate from both sides of C1 and reattach to C2; for relative larger Γ, there appear two symmetrical unstable shear layers.

3. SVS mode

As shown in Fig. 4(c), when the spacing Γ exceeds the critical value Γ_c, the SVS mode is characterized by the vortices synchronously shedding from both the anterior and posterior cylinders. A typical tidiness vortex street is formed behind C1 and C2. The STE pictures for positions A, B, and C demonstrate that the frequencies at different positions are identical and the frequency undergoes a sudden jump at the transition from SLR to SVS mode.

The SBB, SLR, and SVS modes described above have been observed and well studied in early literatures. Further, we will present another flow mode which has never been reported before.

4. SVF mode

For two tandem cylinder with a relative wider spacing Γ that is much larger than Γ_c, a flow mode as shown in Fig. 4(d) is found. Comparing Fig. 4(d) with Fig. 4(c), although there are vortices shedding from the two cylinders synchronously in both the modes, it is noticed that evident distinction exists in the wake behind the posterior cylinder C2. In the SVS mode in Fig. 4(c), a standard Karman vortex street is visualized. However, in the wake of C2 in Fig. 4(d), a shear layer emerges in the middle of the vortices. We can see oblate vortices with the same sign arranged in-line on each side of the shear layer. In particular, as the vortices evolve downstream, the neighboring vortices in each row merge with each other and form a secondary vortex street with a lower frequency and a larger scale in the far downstream wake. We call this pattern SVF mode for the secondary vortices formation. Because of the merging process, the fre-
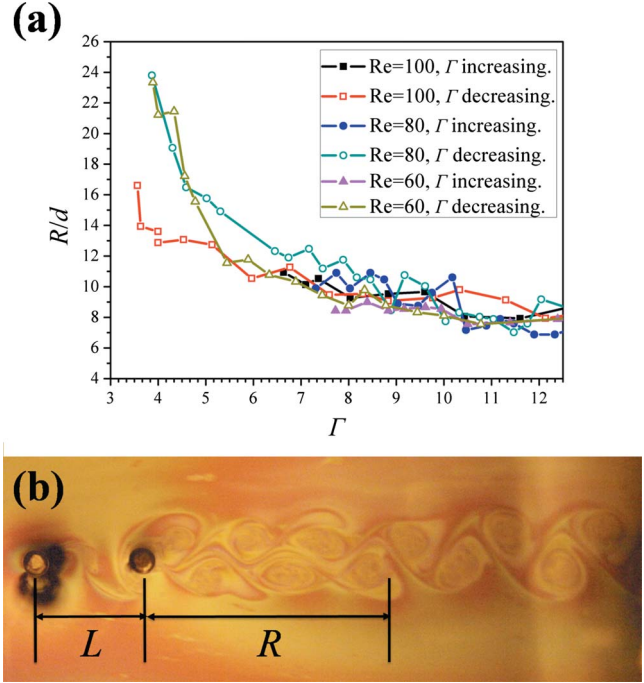

FIG. 5. (Color online) R/d-Γ relations in SVF mode. (a) R/d-Γ curves and (b) definition of R.

quency measured at position C is about half of those at positions A and B.

B. Onset of the secondary vortex street in SVF mode

The in-between shear layer emitted from the downstream surface of C2 becomes a characteristic indicator of SVF mode. When the mergence of neighboring vortices takes place, the shear layer disappears and simultaneously the secondary vortex street forms. The average length of the shear layer is denoted as R and is a function of the spacing Γ. Figure 5 shows the variation of the nondimensional shear layer length R/d with Γ at different Re numbers.

It is seen from Fig. 5 that R/d decreases as Γ increases and the influence of Re is not evidence. With Γ increasing, the vortices and the shear layers become weakened and the vortices are easy to merge. Correspondingly, the R/d will decrease with the increasing Γ. Moreover, we can find the hysteretic phenomenon here. When the spacing Γ increases, the SVF mode replaces the SVS mode at $\Gamma = 6 \sim 7$ and the value of the nondimensional length R/d decreases slightly from about 10 to 7. However, when the spacing Γ decreases from 12, the transition from the SVF to SVS does not occur at $\Gamma = 6 \sim 7$. Instead, the SVF mode maintains and R/d increases to over 20 until the SVS mode appears at $\Gamma = 3 \sim 4$. The hysteresis will be discussed in detail in Sec. VI.

IV. NUMERICAL SIMULATIONS

The information provided in the soap film experiment is somewhat insufficient to analyze the flow phenomena. In order to learn more about the mechanism of SVF mode, we exploited a numerical simulation to deal with this problem.
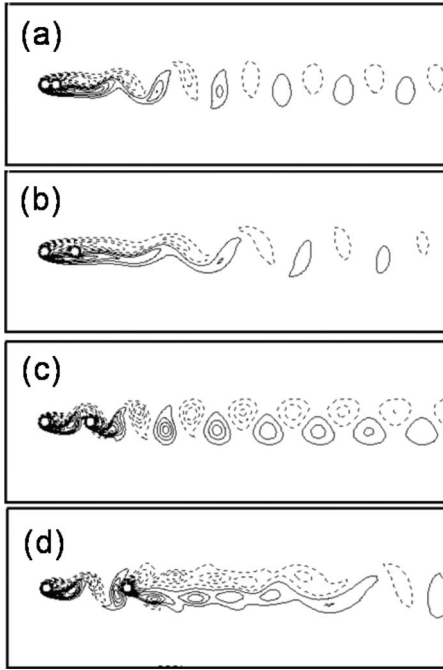
FIG. 6. Vorticity contours. (a) SBB, (b) SLR, (c) SVS, and (d) SVF. Contour levels are from $\omega_{min} = -20$ to $\omega_{max} = 20$ with $\Delta\omega = 0.4$. Dashed lines——negative (clockwise), solid lines——positive (counterclockwise) vorticity.

The two-dimensional incompressible Navier-Stokes equations were solved using a space-time finite element method [30]. The program code has been fully validated in our previous works [31,32]. In our calculation, the domain size is $40d$ in x direction and $18d$ in y direction with $3 \sim 4 \times 10^4$ elements, and the nondimensional time step is chosen as $dt = 0.05$.

Figures 6(a)–6(d) show the vorticity contours in four typical cases at Re=100, corresponding to the SBB ($\Gamma = 1.1$), SLR ($\Gamma = 3.0$), SVS ($\Gamma = 4.5$), and SVF ($\Gamma = 8.0$) modes, respectively. The solid and dashed lines represent positive (counterclockwise) and negative (clockwise) vorticity values. The flow patterns are well consistent with the experimental ones shown in Figs. 4(a)–4(d). In the case of SVF mode, we analyze the formation of the secondary vortex street in the wake of C2 and show the vortex merging process in Fig. 7.

The evolutional process of two neighboring vortices (marked by the ellipse) is shown in Fig. 7. The sequence begins at the bottom left panel and is arranged in the clockwise direction. We can see positive and negative vortices rank in-line by each side of the middle shear layer in the near wake behind C2. On the way of the vortex street moving downstream, the vortex intensity decays and the mergence occurs. Finally, a vortex street with larger scale and lower frequency forms in the far wake.

The numerical results also indicate that the flow modes seriously affect the aerodynamic loads on both the cylinders. Table I shows the average and the time-dependent forces on the two cylinders at Re=100. The forces of a single cylinder at the same Re are also given for comparison.

As shown in Table I, in all the cases of two tandem cylinders, the averaged lift coefficient C_l of every cylinder is
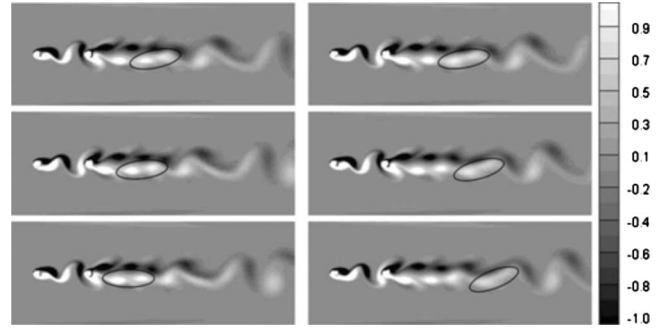

FIG. 7. Sequence plots of the vortex-merging process. The sequence begins at the bottom left panel and may be followed clockwise through the remaining panels.

zero and the averaged drag coefficient C_d is smaller than one on the single cylinder. The downstream cylinder C2 always suffers a smaller drag than C1, especially in the SBB and SLR modes. In these two modes, C2 receives a thrust because of the circumfluence in the region between the two cylinders. In general, the fluctuations of the time-dependent forces on C1 are much smaller than that in the case of a single cylinder, while the fluctuating values on C2 are also smaller in the SBB and SLR modes, but larger in the SVS and SVF modes.

Comparing with the forces in the SVF and SVS modes, we can learn that the formation of the secondary vortex street has little influence on C1. However, both the average and fluctuating values of the drag on C2 are diminished in the SVF mode and the unsteady lifts on both the cylinders are also decreased obviously. It means that the SVF mode is inclined to reduce the unsteady loads on both the cylinders and the drag on the downstream one.

V. MECHANISM OF SECONDARY VORTEX FORMATION

Researchers have devoted their effort to study the secondary vortex street structures including the far wake of a stationary cylinder located in a uniform stream as well as the wake behind an oscillating cylinder in a uniform flow or the wake of an unforced cylinder in a flow excited by external signals. Taneda [33] first observed the wake of a stationary cylinder in a uniform stream by flow visualization. In his experiment, the primary Karman vortex street decays in the downstream and the secondary vortex street forms in the far wake with a larger scale and a lower frequency. Cimbala *et al.* [19] observed the far wakes of two-dimensional bluff bodies at $70 < \text{Re} < 2000$ using smoke-wire visualization and hot-wire anemometer and concluded that the secondary vortex street is independent of the scale or frequency of the primary Karman vortices. This problem was also analyzed numerically by Karasudani and Funakoshi [34]. Recently, Vorobieff *et al.* [35] performed soap film experiments and found that the onset position of the secondary vortex depends on the Reynolds number and the secondary wake begins around $80d$ downstream at Re=100. Those investigations indicate that the formation of the secondary vortex street is due to the hydrodynamic instability of the developing wake profile.

TABLE I. The forces on the cylinders at Re=100.

	SBB	SLR	SVS	SVF	Single
C_d on C1	1.33 ± 0.00	1.25 ± 0.00	1.41 ± 0.02	1.42 ± 0.01	1.48 ± 0.14
C_d on C2	-0.13 ± 0.00	-0.06 ± 0.00	0.91 ± 0.23	0.74 ± 0.10	
C_l on C1	0.00 ± 0.01	0.00 ± 0.04	0.00 ± 0.49	0.00 ± 0.40	0.00 ± 1.18
C_l on C2	0.00 ± 0.06	0.00 ± 0.08	0.00 ± 1.70	0.00 ± 1.38	

On the other hand, Matsui and Okude [36] conducted experimental investigation on the wakes behind a forced cylinder, in which the wakes were excited acoustically with a 1/2 or 1/3 frequency of the primary vortex street. They found that every two or three vortices merge regularly depending on the exciting frequency. Aref and Siggia [37] also observed the formation of the secondary vortex street by introducing subharmonic perturbations to the vortex rows, which was illustrated again by Meiburg [38] in terms of the numerical results. Williamson and Prasad [39] studied the effects of the free-stream disturbances on the wake and showed that the far wake is very sensitive to the free-stream disturbances. The vortex merging phenomena are also observed when a circular cylinder is oscillating horizontally, vertically, or rotationally in uniform flow [40–42]. Those investigations indicate that the external excitation is the origin of the formation of the secondary vortex street and the wake merging plays a critical role.

Let us come back to the SVF mode of the flow around two tandem cylinders in the present work. Unlike the cases of unforced and forced cylinder mentioned above, the downstream cylinder C2 faces to a periodic Karman vortex street in the wake of C1. For the different flow conditions, the flow pattern around C2 is entirely different from that of a stationary cylinder in the uniform flow. Considering the exciting disturbance of the flow or the fluctuation of the cylinder, the relative velocity in the case of a forced cylinder is similar to that of C2. But there are still distinct differences in the wake patterns. In the cases of oscillating cylinder, the wake evolution is that the primary Karman pattern in the near wake transits to a shear layer containing vortices and subsequently the vortices merge to form the secondary vortex street. Whereas in the present SVF mode, the near wake of C2 initially shows two parallel lines within close-packed vortices and then evolves to the large scale vortices.

To reveal the mechanism of the wake formation, we studied the flow field around C2 in the SVS and SVF modes in detail in terms of the numerical results. As shown in Fig. 8, the left column indicates the flow structures around C2 in SVF mode and the right the patterns in SVS mode at the same moment. We can see the similar vortex motion in both the modes including that the vortex V1 shedding from C1 impinges onto C2, combines with the vortex V2 on the surface of C2, then forms a new vortex V3, and sheds downstream. However, there are slight differences in the position of V1 and the relative phase between V1 and V2 when the combination occurs. In SVF mode, because of the much wider distance Γ between the cylinders, V1 is significantly weakened and diffused when it comes to C2. The vortex combination of V1 and V2 happens at the more sideward

surface of C2. After combination, the new positive vortices V3 are suppressed underside and the negative vortices are limited upside in the downstream way, resulting in that oblate vortices come up and arrange in-line. Finally two rows of contrary vortices emerge as shown in Fig. 4(d). In SVS mode, after the vortex V1 combines with V2 on C2, as shown in the right column, the new counterclockwise vortex V3 shifts up to interact with the previous shed clockwise vortices, forms an orbicular vortex, and finally departs from C2. The alternately arranged vortices with opposite sign ultimately make a standard Karman vortex street in the wake of C2. The animations [43] of wake evolution also reveal that the different relative position of V1 and V2 makes tiny discrepancy in their combination process on the downstream cylinder surface and then produces different wake patterns.

VI. MODE TRANSITIONS AND HYSTERESIS

Figure 9 shows the dependence of the Strouhal number Sr on the spacing Γ at Re=80. With Γ increasing, different modes and Sr-Γ curvers are shown in Fig. 9(a). At $\Gamma=1$, no gap exists between the two cylinders, the value of Sr measured at Position B is about 0.15, equal to the value in the case of a single cylinder at Re=80. As Γ increases, the SBB mode retains and Sr drops rapidly to 0.11 until $\Gamma=1.8$. As Γ further increases, the flow pattern enters SLR mode, in which Sr basically keeps unchanging. Once Γ exceeds the critical value Γ_c, the upstream cylinder C1 starts to shed vortices and the flow enters SVS mode. The value of Sr gains up imme-
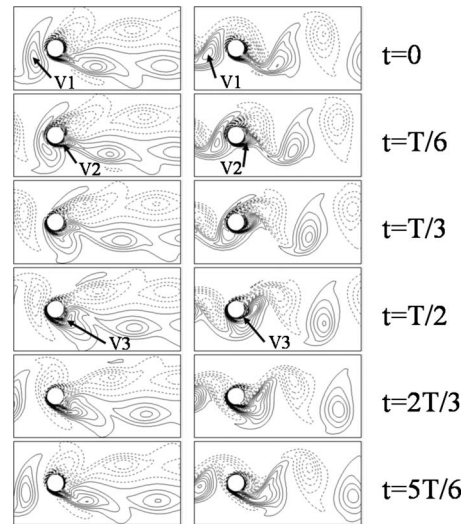

FIG. 8. Vorticity contours around C2 in SVF (left) and SVS (right) modes. Contour levels are the same as in Fig. 6.
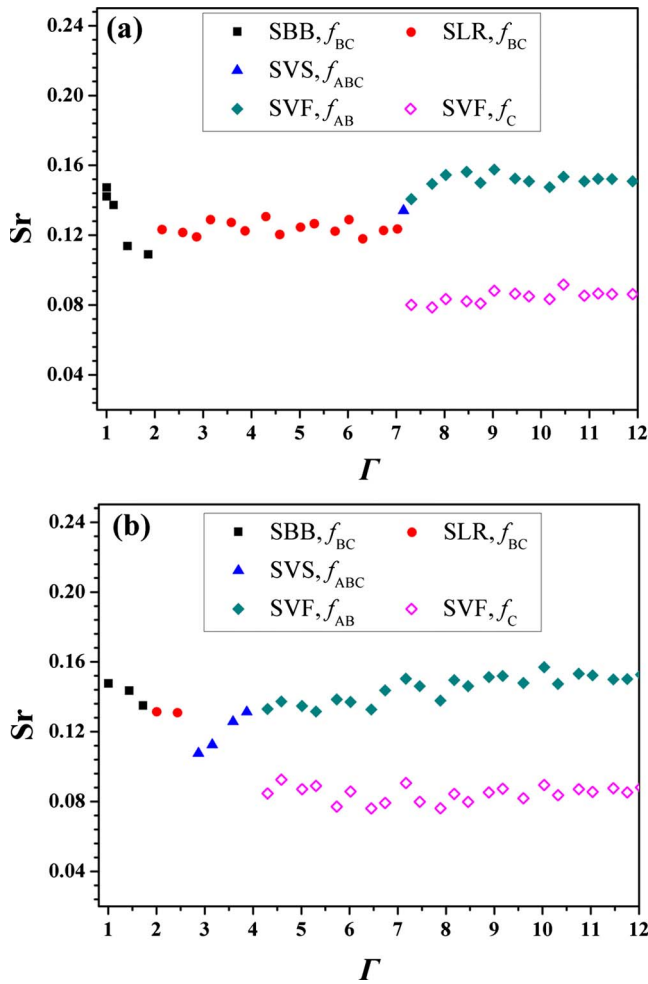
FIG. 9. (Color online) The Sr-Γ relations at Re=80. (a) Γ increases. (b) Γ decreases.

FIG. 10. (Color online) Distribution of modes in (Γ, Re) plane. (bar—SBB and SLR, solid circle—SVS, solid right triangle—SVF modes in Γ increasing process; open square—SBB and SLR, open circle—SVS, open left triangle—SVF modes in Γ decreasing process. Thin solid line—Γ_c^+, thin dashed line—Γ_m^+, thick solid line—Γ_c^-, thick dashed line—Γ_m^-.)

10 shows the distribution of modes in (Γ and Re) plane. The hysteresis is observed in the range between the critical boundaries Γ_c^- and Γ_m^+, where the superscripts + and − denote the critical values in the increasing and decreasing ways, respectively. When Γ increases, a narrow region exists between the thin solid line Γ_c^+ and dashed line Γ_m^+, which means that the SVS mode retains for a short time and transfers to the SVF mode quickly. However, when Γ decreases, the region between the thick solid line Γ_c^- and dashed line Γ_m^- is much wider, which means the SVS mode occurs in a wider spacing range.

The critical value Γ_c for the transition between SLR and SVS modes is considered to be about 3.0–4.0 in previous work, depending on Re and the experimental conditions. For instance, Γ_c is 5 at Re=80 and 3 at Re=3400 in the experiments of Tanida *et al.* [3] In numerical results of Didier [16], the value of Γ_c at Re=100 is ascertained to 3.95–4.0. Kuo *et al.* [11] studied the transition between the SLR and SVS modes in detail in his experiments, and found that two symmetric unstable shear layers appear between the two cylinders at $4.5 < \Gamma < 5.5$ and the upstream cylinder starts to shed vortices at $\Gamma_c = 6.0$ at Re=1000. In our numerical simulation of two tandem stationary cylinders, the results show that Γ_c is 3.5–4.0 and Γ_m is 6.0–6.5. Mizushima and Suehiro [17] first predicted the existence of hysteresis around the critical spacing $\Gamma_c = 3.05–3.4$ through stability analysis and numerical simulations. Tasaka *et al.* [18] confirmed the modes overlapping at $\Gamma_c = 4.6–5.0$ when Γ is fixed and Re is changed. In our experiments (see Fig. 10), when Γ increases, Γ_c^+ is 6.6, 6.9, and 7.5 for Re=100, 80, and 60, respectively, much larger than the value 3.0–4.0. When Γ decreases, Γ_c^- is 2.5, 2.6, and 3.0 for Re=100, 80 and 60, respectively, much smaller than the previous values. We also noticed that the critical values are larger for smaller Re, consistent with the early research. Simulations of the processes with Γ increasing and decreasing at a very small velocity were also carried

diately to 0.15 at Γ_c. As Γ increases, the SVS mode is unabiding and transits rapidly to SVF mode at Γ_m, where Γ_m denotes the transition spacing between SVS and SVF modes. In SVF mode, the frequency at Position B is equal to that at Position A, but it is much larger than the value at Position C. The values of Sr based on f_B and f_C in SVF mode are both drawn in Fig. 9, we can find that the value of Sr based on f_C is almost half of that on f_A and f_B.

As mentioned in Sec. III, in the Γ decreasing process the transition from SVF to SVS mode takes place at a much smaller Γ_m than in the Γ increasing process [see Fig. 9(b)]. The transition spacing Γ_c between SVS and SLR modes also indicates the hysteretic phenomenon. As shown in Fig. 9, both the critical values and the range of each mode are obviously different in the two processes. This hysteresis reflects the different mechanisms of mode transitions. When Γ increases, Γ_c presents the process for the shear layers separated on the surface of C1 from reattaching to vortex forming, whereas in the Γ decreasing process, the existed vortex shed from C1 is supposed to be suppressed at Γ_c. Similarly, the transition spacing Γ_m in Γ increasing and decreasing processes present the formation and disappearance of the secondary vortex street, respectively.

The Sr-Γ relationships and the mode transitions at Re=100 and 60 indicate the same hysteretic phenomena. Figure
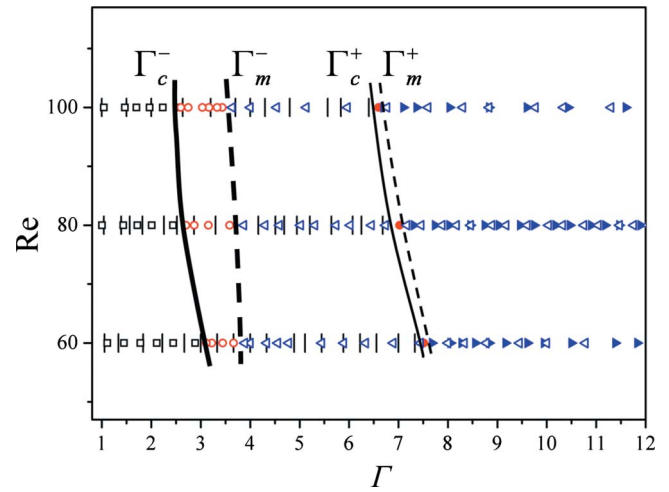
out and our numerical results also confirmed the existence of hysteresis. The numerical results show $\Gamma_c^+=5.0$, $\Gamma_m^+=7.5$ and $\Gamma_m^-=6.5$, $\Gamma_c^-=3.0$ at Re=100.

There seems to be some evident discrepancies between the results of different experiments and computations. A reason for the discrepancies may source from the different initial conditions. Although the final state of Γ and Re are the similar, the flow field will be different when the initial condition is different. Generally, the influence of the initial condition is ineluctable. In laboratory, the models are installed in the test section in advance and then the velocity in the test section starts from rest to a stationary speed. In numerical simulation, the calculation begins from the flow field at rest and is converged to the stationary state. In addition, in the research of hysteresis, the changing way of the parameter Re or Γ may make different initial conditions of the flow field, and the changing rate will also have effect on the results. In experiments in the water tunnel [18], the spacing Γ was fixed and the flow speed was changed, whereas in our experiments Γ changed at a fixed Re. It seems to us that some inconsistent results are understandable.

VII. CONCLUSIONS

Experiments on two tandem circular cylinders at Re=60, 80, and 100 were conducted in a soap film tunnel, in which the nondimensional spacing Γ between the cylinders was changed in two contrary ways, increasingly and decreasingly. Four flow modes were classified, in particular a SVF mode was first put forward, which is characterized by the parallel close-packed vortices rows in near wake and the formation of secondary vortex street in far wake of the downstream cylinder. A space-time finite element method was applied to study the mechanism of the SVF mode and the mode exchanges numerically. The dependence of the Strouhal number Sr on the spacing Γ and hysteretic phenomena were also studied. The main conclusions are briefly summarized as follows:

(1) With Γ increasing, in addition of the successive SBB, SLR, and SVS modes, another SVF mode was observed at large Γ in our experiments, in which a secondary vortex street forms in the far wake behind the downstream cylinder.

(2) The averaged drag of each cylinder for all modes was diminished comparing with an isolated cylinder. The upstream cylinder always suffers smaller unsteady loads and larger averaged drag with respect to the downstream one. The downstream cylinder in the SBB and SLR modes obtains a thrust in the flow. Comparing with the SVS mode, the SVF mode helps to reduce the unsteady loads on both the cylinders and the drag of the downstream cylinder.

(3) The Strouhal number Sr depends strongly on Γ and an evident jump occurs at the transition between the SLR and SVS modes. Sr-Γ relation is obviously different among the modes.

(4) The critical spacing values Γ_c and Γ_m are related not only to the Reynolds number Re but also to the changing way of Γ. Hysteretic phenomena of mode exchanges were observed when we increased or decreased the cylinder spacing continuously at a fixed Re.

[1] M. M. Zdravkovich, Aeronaut. J. **76**, 108 (1972).

[2] M. M. Zdravkovich, J. Fluids Struct. **1**, 239 (1987).

[3] Y. Tanida, A. Okajima, and Y. Watanabe, J. Fluid Mech. **61**, 769 (1973).

[4] T. Igarashi, Bull. JSME **24**, 323 (1981).

[5] T. Igarashi, Bull. JSME **27**, 2380 (1984).

[6] D. Sumner, S. J. Price, and M. P. Paidoussis, J. Fluid Mech. **411**, 263 (2000).

[7] J. C. Lin, Y. Yang, and D. Rockwell, J. Fluids Struct. **16**, 1059 (2002).

[8] M. M. Alam, M. Moriya, K. Takai, and H. Sakamoto, J. Wind. Eng. Ind. Aero. **91**, 139 (2003).

[9] G. Xu and Y. Zhou, Exp. Fluids **37**, 248 (2004).

[10] Y. Zhou and M. W. Yiu, J. Fluid Mech. **548**, 17 (2006).

[11] C. H. Kuo, S. M. Chein, and H. J. Hsieh, Exp. Fluids **44**, 503 (2008).

[12] S. Mittal, V. Kumar, and A. Raghuvanshi, Int. J. Numer. Methods Fluids **25**, 1315 (1997).

[13] J. R. Meneghini, F. Saltara, and J. A. Ferrarijr, J. Fluids Struct. **15**, 327 (2001).

[14] B. Sharman, F. S. Lien, L. Davidson, and C. Norberg, Int. J. Numer. Methods Fluids **47**, 423 (2005).

[15] P. F. Zhang, J. J. Wang, and L. X. Huang, App. Ocean Res. **28**, 183 (2006).

[16] E. Didier, C. R. Mec. **335**, 696 (2007).

[17] J. Mizushima and N. Suehiro, Phys. Fluids **17**, 104107 (2005).

[18] Y. Tasaka, S. Kon, L. Schouveiler, and P. L. Gal, Phys. Fluids **18**, 084104 (2006).

[19] J. M. Cimbala, H. M. Nagib, and A. Roshko, J. Fluid Mech. **190**, 265 (1988).

[20] Y. Couder, J. M. Chomaz, and M. Rabaud, Physica D **37**, 384 (1989).

[21] J. M. Chomaz and B. Cathalau, Phys. Rev. A **41**, 2243 (1990).

[22] P. Vorobieff, D. Georgiev, and T. Shakeel, *Advances Fluid Mechanics* (WIT Press, Southampton, 2002), Vol. IV.

[23] D. Georgiev and P. Vorobieff, Rev. Sci. Instrum. **73**, 1177 (2002).

[24] A. A. Trapeznikov, Proceedings of the Second International Congress on Surface Actuators, 1957 (unpublished), pp. 242–259.

[25] J. M. Chomaz, J. Fluid Mech. **442**, 387 (2001).

[26] P. Vorobieff and R. E. Ecke, Phys. Rev. E **60**, 2953 (1999).

[27] L. B. Jia, F. Li, and X. Z. Yin, J. Fluid Mech. **581**, 199 (2007).

[28] A. Roshko, Nat. Adv. Comm. for Aero, Report 1191 (1954).

[29] P. Roushan and X. L. Wu, Phys. Rev. Lett. **94**, 054504 (2005).

[30] T. E. Tezduyar, M. Behr, S. Mittal, and J. Liou, Comput. Meth-

ods Appl. Mech. Eng. **94**, 353 (1992).

[31] G. J. Dong and X. Y. Lu, Int. J. Numer. Methods Fluids **48**, 1351 (2005).

[32] G. J. Dong and X. Y. Lu, Phys. Fluids **19**, 057107 (2007).

[33] S. Taneda, J. Phys. Soc. Jpn. **14**, 843 (1959).

[34] T. Karasudani and M. Funakoshi, Fluid Dyn. Res. **14**, 331 (1994).

[35] P. Vorobieff, D. Georgiev, and M. S. Ingber, Phys. Fluids **14**, L53 (2002).

[36] T. Matsui and M. Okude, IUTAM Sym. Struct. Comm. Turb. Shear Flows, Report 156 (1983).

[37] H. Aref and E. Siggia, J. Fluid Mech. **109**, 435 (1981).

[38] E. Meiburg, J. Fluid Mech. **177**, 83 (1987).

[39] C. H. K. Williamson and A. Prasad, J. Fluid Mech. **256**, 269 (1993).

[40] P. W. Bearman, Annu. Rev. Fluid Mech. **16**, 195 (1984).

[41] O. Inoue and T. Yamazaki, Fluid Dyn. Res. **25**, 1 (1999).

[42] F. L. Ponta and H. Aref, J. Fluids Struct. **22**, 327 (2006).

[43] See supplementary material at http://link.aps.org/supplemental/10.1103/PhysRevE.81.036305 for the animations of numerical wake evolutions in SVS and SVF modes.